https://doi.org/10.1016/j.jmst.2020.05.065

Research Article

Critical transitions in the shape morphing of kirigami metallic glass

D.X. Han [1], L. Zhao [1], S.H. Chen [2], G.Wang [3], K.C. Chan [1*]

[1] Department of Industrial and Systems Engineering, The Hong Kong Polytechnic University, Hong Kong

[2] School of Mechanical Engineering, Hefei University of Technology, Hefei 230009, China

[3] Laboratory for Microstructures, Institute of Materials, Shanghai University, Shanghai 200444, China

*Corresponding author. Prof., Ph.D.; Tel.: +852 96696725

E-mail address: kc.chan@polyu.edu.hk (K.C. Chan)

Kirigami, the ancient Japanese paper cutting technique, has been applied to achieve high stretchability and low energy loss of designed metallic glass. Despite the exploration of the underlying deformation mechanism of kirigami-inspired structures from the energy point of view, the morphable responses of the kirigami patterns and the origin of the kirigami response are yet to be fully understood. This study reveals the mechanical driven-forms of the kirigami structure with the corresponding deformation stages. Based on beam deflection theory, the elastic buckling behavior of kirigami metallic glass is manifested and a critical force prediction model is developed. Moreover, a force concentration parameter is introduced in the rigid-plastic deformation stage, predicting the nominal ultimate force. The kirigami-inspired facture force is firstly proposed. The findings of these models are in good agreement with the experimental size-dependent kirigami responses, and expected to provide significant insights into the understanding of the deformation behavior and the design of kirigami metallic glasses.

Keywords: Metamaterial; Kirigami metallic glass; Critical load; Size effect; Beam deflection

1. Introduction

Metamaterials circumvent the intrinsic limits of mechanical properties of materials (e.g., low deformability and low shape tenability), opening up a new avenue for extraordinary mechanical properties, such as superelasticity [1], shape morphing [2, 3], negative Poisson's ratio [4, 5]. Inspired by architected material, kirigami has been introduced in metamaterial design. Kirigami, originating from the ancient paper cutting in Japan, is an easy and cost-effective method that can be applied to materials for achieving extremely large stretchability [6-9].

Kirigami inspired structure has been applied in traditional materials such as fabrics [10], kaptons [11] and metals [12], along with advanced materials including graphene [13], shape memory polymers [14, 15], and hydrogels [16]. Various potential applications for these Kirigami structures have also been explored including fabric kirigami heater for soft actuators, kapton kirigami sheet for integrated solar tracking, kirigami-based graphene for biological sensing, and shape memory polymer kirigami open-honeycomb for vibration-driven application. Metallic glasses, being strong and stiff materials with the short-to-medium-range order atomic packing [17-19], have been used for kirigami structures as well. The kirigami metallic glasses have demonstrated superior stretchability with low strain energy loss and large elastic strain [20, 21]. Chen's study revealed that the strain energy losses of kirgami metallic glasses (< 3%) [20], are much smaller than those of kirigami crystalline polyimides (~18%) [22]. Besides, the elastic strains of kirigami metallic glasses were shown to be almost 3 times that of stainless steels [20]. The kirigami metallic glasses demonstrate a great potential in the application of reversible mechanical devices.

Due to their outstanding stretchability, the mechanical behaviors of kirigami based structures have been widely investigated. Lin and Yang reported that the local cut and the global hierarchical pattern significantly affect the tensile strength of the kirigami structures [23, 24]. Qi correlated the fracture strain with the cuts density and the ratio of cut length to ribbon length, based on atomistic simulations [25]. Wang's study revealed that not only the kirigami pattern but also the sample geometric parameter has significantly effects on the mechanical performance (e.g., energy absorption) [26]. On

the other hand, some researchers have investigated the kirigami-inspired deformation mechanisms. Saito's work revealed that the kirigami-inspired deformation behavior is composed of in-plane and out-of-plane process [27]. Whereas the different deformation stages, Kotov's group reported that the trend of the critical load in post-buckling deformation stage is influenced by different kirigami unit geometries, and suggests that the trend is caused by the variation of the material rigidity [22]. Moshe's group further showed that the kirigami unit, taken as a single square frame, acts as a geometrically tunable source of local stress under load [28, 29]. However, the kirigami-inspired deformation mechanisms are still not fully understood, and some fundamental issues, including the origination of the parameter effect and the model for describing critical deformation response, need to be further answered. In the present work, in order to address these issues, the kirigami-inspired deformation mechanisms, especially the critical transitions in force responses of different deformation stages, are investigated.

Our work applies ten scaled kirigami patterns to study the deformation responses of kirigami metallic glass. A beam deflection mechanism is introduced in the analyses of the transition during elastic deformation stages. Inspired by the stress concentration factor, the intensity of the force concentration that gives a prediction of the relationship between the fracture force and the kirigami geometric size is introduced in the analyses of plastic deformation behavior. The critical force prediction model at the micrometer scale, which is verified by the kirigami response of the scaled samples, is proposed. The study reveals for the first time (1) the relationship of the intrinsic material properties and external geometric parameters with the critical deformation response; and (2) the size effect in the kirigami metallic glass. The models developed in this study can be applied to the design of kirigami structures for other materials.

2. Experimental Methods

The Fe-based metallic glass with a composition of $Fe_{78}Si_9B_{13}$ (at.%) was chosen as the model material, due to its wide functional applications [30, 31] and well-studied mechanical properties [32, 33]. The $Fe_{78}Si_9B_{13}$ ribbons with a thickness of 40 μm were photochemical machined (PCM) to obtain kirigami samples with ten different scaled unit sizes. Details of the samples were shown in Fig. 1, where $L_1 = 6.5L_0$, $L_2 = 12L_0$, L_0

= U_0, and 2r arounds 0.06 mm, while the number of arrays of the cuts was fixed to 25, W was fixed to 8 mm. U_0, was set to be 150 μm, 225 μm, 300 μm, 375 μm, 450 μm, 525 μm, 600 μm, 675 μm, 750 μm, and 900 μm. The samples with the ten different scaled unit sizes are shown in Figs. 1(b)-(k).

Tensile tests were conducted using the Instron 3344 single column system, with load force resolution, displacement resolution, and data acquisition frequency of 50 nN, 2×10^{-2} nm, and 50 s^{-1}, respectively. The tensile loads were executed at a strain rate of 10^{-2} s^{-1}, and the real-time video was recorded for characterizing the corresponding deformation features of the samples. At least three repeatable tensile tests were performed for the samples with the same geometric pattern.

The Finite Element Method (FEM) simulation was carried out to give the guidance for stress distribution in the kirigami-inspired deformation. The buckling mode with an additional perturbation was conducted in the early elastic deformation process. The force control model which is in the length arithmetic was conducted in the post-buckling behavior. The adapted metallic glass parameters, yield stress, Young's modulus, and Poisson's ratio, are 3.212 GPa [34], 165 GPa [34], and 0.32 [35], respectively.

3. Theory modeling

Tensile force induces the kirigami patterns to transform from 2D creases to 3D approximate rhombuses. Considering a typical pattern designed with L_1/U_0 = 6.5 and L_2/U_0 = 12, the deflected rhombic pattern during the kirigami mechanical response is shown in Fig. 2. Referring to Fig. 2(b) and Fig. 2(c), the side of the rhombic tension patterns can be taken as two connected cantilever beams with concentrated load acting upwards or downwards at each other's end respectively. When the beam is deflected, a rotation is observed, shown in Fig. 2(d). Based on the curve of the beam deflection, we get:

$$\gamma d\theta = ds \tag{1}$$

where γ is the curvature radius, θ is the rotation angle of the beam in radians in this study, and s is the distance along the deflection curve between beam points. Consequently, the curvature k, the reciprocal of the curvature radius, is given by:

$$k = 1/\gamma = d\theta/ds \tag{2}$$

In the deflection of beam, the bending moment M is taken as [36]:

$$M = \int \sigma_x y dA \tag{3}$$

where σ_x is the horizontal stress acting on the cross section, dA is the element area perpendicular to σ_x, and $\sigma_x dA$ is the element force acting on the element area. Based on the Hooke's law, $\sigma_x = E\varepsilon_x$ for the linearly elastic beam material. And due to the strain-curvature relation [37], $\varepsilon_x = ky$, where ε_x is the longitudinal strain in the beam, y is the distance from the neutral surface in vertical direction, equation (3) derived as:

$$M = \int E\varepsilon_x y dA = \int E(ky) y dA = kE \int y^2 dA \tag{4}$$

where E is Young's modulus of the beam material. Considering $I = \int y^2 dA$ [35], equation (2) is taken as:

$$d\theta/ds = M/(EI) \tag{5}$$

where I is moment of inertia which reveals the geometrical properties [38-40], EI is the flexural rigidity of the beam [41], i.e. the resistance of the beam to bending [42].

4. Results

4.1. Kirigami-inspired tensile response

The load-strain curves of the kirigami metallic glass are shown in Fig. 3, which reveals three deformation stages. For stage 1, an extremely fast load rise occurs at the very beginning of the deformation process. The increase of load then becomes relatively gentle at stage II. When the specimen is further stretched to stage III, the increase of load becomes rapid. However, the increase of load in stage III is not as fast as that in stage I. Stage I was in-plane deformation, and, both stage II and stage III were out-of-plane deformation with a locally deformed rhomboid pattern, as shown in Figs. 3(c) and 3(d). Further, the deformation in stage II is in a dramatic softening and rotation state with a reduction in slope compared with that of stage III, i.e., a small increase in load force induces a large tensile strain. The deformation in stage III is in a plastic stiffening state, differing from the former two stages which are in elastic linear deformation. The kirigami response is a mechanics driven process, exhibiting critical transitions in deformation. Induced by the loading force, the transition from 2D planar to 3D tensile structure in stage I is marked as P which is the transition point of the slope

of strain-load in the kirigami-inspired elastic deformation process as shown in Fig. 3(a). The loading force continues to induce the transition of the out of plane deformation from a linear state to non-linear state corresponding to the transition from softening tension to stiffening stretching, and the transition is marked as point Q in Fig. 3(a). With the increasing loading force, fracture occurs and is marked as point R in Fig. 3(a). The transition force from the in-plane deformation to the out-of-plane soft deformation, the transition force between the out-of-plane soft deformation and out-of-plane rigid deformation, and, the fracture force of the out-of-plane rigid deformation, which are shown in Fig. 3(a), corresponds to $F_{I_{ult.}}$, $F_{II_{ult.}}$, and $F_{III_{ult.}}$, respectively. In the tensile behavior, the rhomboid, the tunable source of the deformation response, is taken as a kirigami pattern unit. The rhomboid hole can be taken as a combination of beams whose deflection, rotation, and tension affect the kirigami-inspired deformation response, detailed analyses of which are given in the discussion section.

4.2. Size-dependent critical transition in tensile response

The load-strain curves of kirigami patterns scaled with different unit sizes are presented in Fig. 4(a). Fig. 4(a) shows that the larger unit size samples, the larger ultimate fracture force. To give a closer comparison, the representative load-strain curves of tensile tests with the same unit size are exhibited in Fig. 4(b). The samples with small unit sizes present large critical deflection force in stage I and large soft-rigid transition force in stage II. Further, the smaller the unit size, the larger the slope in stage II, while the slopes are almost unchanged in stage III, as shown in Fig. 4(b).

The absolute load forces of stage I, stage II, and stage III are identified as $F_{I_{ult.}}$, ($F_{II_{ult.}}$ - $F_{I_{ult.}}$), and ($F_{III_{ult.}}$ - $F_{II_{ult.}}$), respectively. Fig. 5 shows both the absolute load force of stage I and stage II decreases with increasing unit size, while that of stage III increases as unit size increases. The power law equation $y = ax^b$ [43, 44] is applied as the fitting function, as shown in Fig. 5. Fig.5 shows that the absolute force of the in-plane deformation is scaled with $1/U^{0.91 \pm 0.08}$ ($\sim 1/U_0$); the absolute force of the out-of-plane soft deformation process is scaled with $1/U^{0.86 \pm 0.05}$ ($\sim 1/U_0$); while the

absolute force of the out-of-plane rigid deformation process is scaled with $U_0^{0.41 \pm 0.07}$, having a different dependency between the absolute force and the unit size compared with the initial two stages.

The strain-load slopes in stage II are plotted as a function of unit sizes, as shown in Fig. 6, revealing that the slope scales with $1/U^{0.87 \pm 0.04}$. The smaller the kirigami unit size, the steeper the slope, i.e. the smaller the kirigami unit size, the larger load growth rate in the out-of-plane soft deformation process, and is qualitatively presented in Fig. 4 as well. In addition, the dependency of the strain-load slopes and kirigami unit size is almost the same as that of $(F_{II_{ult.}} - F_{I_{ult.}})$ and krigami unit size, which indicates that the absolute strain of stage II remains constant in samples with the scaled kirigami unit sizes. The absolute strains in stage II, i.e., $(\varepsilon_{II_{ult.}} - \varepsilon_{I_{ult.}})$, of different kirigami unit sizes are extracted from Fig. 4(a). The absolute strains, which are almost invariable with different kirigami unit sizes, are presented in Table 1. This indicates that the scaled kirigami unit would not change the absolute tensile strain of the out-of-plane soft deformation stage but would affect the load force growth rate per strain, leading to the different absolute force in stage II. It is worth mentioning that the absolute strain of samples with kirigami unit size of 150 μm is much larger that of other unit sizes. This is because the pattern seam size (2r ~ 60 μm, shown in Fig 2(a)) closes to the kirigami unit size of 150 μm, affecting the tension strain in stage II.

5. Discussion and analysis

The beam deflection mechanism that is based on the elastic analysis [45-47] and the stress concentration theory that indicates the localized stress caused by discontinuities in geometry (e.g., notches, holes) [40, 48, 49], are introduced to study the critical response of the deformation behavior in kirigami metallic glass.

5.1. In-plane deformation stage

Considering the deflection curve is almost horizontal, i.e., the rotation angle θ is extra small, at the transition of the tensile response from the in-plane deformation to the out-of-plane deformation, and $\cos\theta = dx/ds$, the following approximation is made:

$$ds \approx dx \tag{6}$$

where x is the distance to the nominal fixed point in the longitudinal direction of the beam, i.e. the coordinate in the x axis in this study, as shown in Fig. 2. With the above approximation, combining equation (2) with equation (6), we get:

$$d\theta/dx \approx d\tan\theta/dx = d^2h/dx^2 \tag{7}$$

where h is the deflection of beam in the vertical direction, i.e., the tensile direction.

Since the beam material is in a linearly elastic state in the in-plane deformation stage, the bean deflection mechanism applies to the kirigami-inspired deformation of this stage. Combining equation (5) with equation (7), the second order differential equation of deflection is arranged as:

$$EI(d^2h/dx^2) = M \tag{8}$$

In this tension test, equation (8) can be expressed as follows:

$$EI(d^2h/dx^2) = F(L' - x) \tag{9}$$

where F represents the force required to induce deflection, L' is the coordinate in the x axis direction where the concentrated load acting on the beam, and can be regarded as the nominal beam length in this study.

Integrating equation (9), the deflection in the tensile test is given as:

$$h = Fx^2(3L' - x)/(6EI) \tag{10}$$

According to equation (10), the deflection at the nominal free end of the beam, δ, is yielded as follows:

$$\delta = FL'^3/(3EI) \tag{11}$$

In this kirigami tensile test, the moment of inertia in the in-plane stage is calculated to be $I = tw^3/12$ where t is the nominal thickness of the deformed beam, w is the nominal width of the deformed beam. Besides, a combined deflection of the two beams constitutes the deflection of a kirigami unit, as shown in Fig. 2(c), making the total deflection in the relationship:

$$\delta_{I.tot.} = \delta_{I.1} + \delta_{I.2} = 8FL'^3/(Etw^3) \tag{12}$$

The nominal beam length in this kirigami deformation process is $(L_2 - L_0)/4$, which is nearly equal to the actual beam length, due to the extremely small deflection in this stage. The nominal beam thickness and the nominal beam width are t_0 and U_0,

respectively, in the in-plane stage. Based on equation (12), the element tension load acting on the nominal element beam is as:

$$F_0 = Et_0\delta_{I.\,tot.}U_0^3 \big/ \{8[(L_2 - L_0)/4]^3\} = 8U_0^3 t_0 E\delta_{I.\,tot.} \big/ (L_2 - L_0)^3 \quad (13)$$

Equation (13) reveals that the critical beam elementary deflection force is dependent both the elastic property of the material, e.g. Young's modulus, and the geometrical factors of the samples, e.g. length, width, and thickness of the beam in the in-plane stage. Considering that the scaled samples with the same geometric characteristics have the same thickness, equation (13) reveals that the deflection force is only affected by, $\delta_{I.\,tot.}$, i.e., the critical deflection displacement in stage I, in this study. According to Ref. [28], the critical deflection displacement in the in-plane frame buckling is found to be proportional to $(t_{fra.}/w_{fra.})^2 L_{fra.}$ when $w_{fra.}/L_{fra.}$ is fixed, where $t_{fram.}$, $w_{fram.}$, and $L_{fra.}$ are the thickness, width, and length of the frame, respectively. In this study, $w_{fram.} = w_{beam} = U_0$, $L_{fra.} = (L_2 - L_0)/2$. Thus, the elementary deflection load is simplified as follows:

$$F_0 = [4U_0 t_0^3/(L_2 - L_0)^2] * E \quad (14)$$

The beam forces in the same row can be added together to become the row force. Resembling a lightweight spring model, the row force, F_{row}, equals to each other in the same column, equaling the load force applied in the kirigami sample, F_I:

$$F_I = F_{row} = NF_0 = \{N[4t_0^3/(m - n)^2]E\}/U_0 = N\Psi E/U_0 \quad (15)$$

where $\Psi = 4t_0^3/(m - n)^2$ is the geometric constant, which remains invariable for the same geometric characteristic of kirigami patterns, and $m = L_2/U_0 = 12$, $n = L_0/U_0 = 1$, in this study; N is the number of beam columns in a row. If the numbers of beam column of a row are different in the kirigami structures, the larger the column number of beams in a row, the larger the critical deflection force required in this row. When a row with the least beam columns starts to deflect, the row with more beam columns is still in the in-plane stage and not reaching its critical deflection force. Thus, in stage I, the critical deflection force is calculated to be:

$$F_{I_{ult.}} = \min(N_1, N_2, \cdots, N_n)\,\Psi E/U_0 \quad (16)$$

The equation (16) predicts the critical deflection force in stage I. The formula reveals that kirigami pattern with small unit size strengthens the critical deflection force during kirigami transition response from in-plane to out-of-pane. The formula predicts the critical deflection force is in proportion to $1/U_0$ in this study, which has good consistency with the experimental data of the scaling unit size of the tensile kirigami samples, i.e., $F_{I_{ult.}} \propto 1/U^{0.91 \pm 0.08}$. It indicates that the beam deflection mechanics gives a good prediction for the critical response of elastic kirigami in-plane deformation.

The beam deflection theory proves that not only the elasticity of the materials, but also the geometric characteristics and the column number of the kirigami pattern affect the deflection behavior. The small length, large width, large thickness, or large the minimum column number in a row of kirigami patterns contributes to a large critical deflection force during the transition mechanical response from in-plane state to out-of-plane soft state.

5.2. Out-of-plane soft deformation stage

The out-of-plane soft deformation, which is the stage from the starting rotation of slight deflection beam to the final rotation of 90° of the curved beam, is in the elastic state. It indicates that the beam deflection theory can still be applied in this stage. The similarity in critical deflection force and absolute soft-rigid transition force dependency on kirigami unit size also suggests a likelihood of the same origin for the ultimate force of stage I and stage II, i.e., the occurrence and accomplishing of the beam deflection dynamics induce the kirigami criticality l response during the in-plane and out-of-plane deformation process. Due to the larger deflection of the curved beam, the assumption of curvature k equaling to d^2h/dx^2 is not appropriate for the out-of-plane deformation stage. The exact expression for curvature is as follows:

$$k = d\theta/ds = [\, d \arctan\, (dh/dx)/dx\,]^* \,(\, dx/ds\,) \qquad (17)$$

Considering $ds^2 = dx^2 + dh^2$, the differentiation of s gives $ds/dx = [1+ (\, dh/dx\,)^2]^{1/2}$. In addition, the differentiation of arctangent equation is taken as $d\, arctan\,(dh/dx)/d\, x = (d^2h/dx^2)/[1 + (dh/dx)^2]$. Thus, curvature for large

deflection yields:

$$k = (d^2h/dx^2)/[1 + (dh/dx)^2]^{3/2} \quad (18)$$

Combine equation (5) and equation (18), we get $\theta(x) = dh/dx = F(2XL' - x^2)/\{2EI\sqrt{1 - [F(x^2 - 2XL')/(2EI)]^2}\}$, leading to

$$\rho(0) = (1 + \theta^2(0))^{3/2}/\theta(0)' = EI'/(FL') \quad (19)$$

Then we obtain:

$$\delta^2_{II.tot..} = (2h_{(L')})^2 = 4(s^2 - L'^2) = 4\left[(\rho\theta)^2 - L'^2\right] = L'^2 * \Gamma_{\left(FL'^2/2EI\right)} \quad (20)$$

where $\Gamma_{\left(FL'^2/(2EI)\right)} = \{4[FL'^2/(2EI)]^2 - 3\}/\{1 - [FL'^2/(2EI)]^2\}$. Considering the invariant strains with different kirigami unit sizes in stage II, which lead to the fixed value $(\delta_{II.tot.}/L')^2$ that is shown in Table 1, $\Gamma_{\left(FL'^2/(2EI)\right)}$ is constant in this study. In stage II, $I_{II} = wt^3/12$, substitute L', w and t for $\cos\theta\,(L_2 - L_0)/4$, U_0, and t_0, respectively. And consider the effect of the designed kirigami patterns on the elementary critical force, the soft-rigid transition force of out-plane deformation process yields:

$$F_{II_{abs.ult.}} = \min(N_1, N_2, \cdots, N_n)\, bEU_0t_0^3/(L_2 - L_0)^2 = \min(N_1, N_2, \cdots, N_n)\Lambda E/U_0 \quad (21)$$

where b is a dimensionless constant, $\Lambda = 32bt_0^3/[3\cos\theta^2(m - n)^2] = (8b/3\cos\theta^2)\,\Psi$.

The deflection beam formula predicts that the absolute force of stage II, i.e. $(F_{II_{ult.}} - F_{I_{ult.}})$, scales with $1/U_0$, which has a good consistence with Fig. 5(b) that is fitted by the power law function, i.e., $(F_{II_{ult.}} - F_{I_{ult.}})$, scales with $1/U^{0.86 \pm 0.05}$. The results support the application of beam defection mechanism in out-of-plane soft response.

5.3. Out-of-plane rigid deformation stage

The good consistency between experiment result and FEM data demonstrate the effectiveness of the FEM in the kirigami tensile test, as shown in Fig. 7(a). The FEM analysis presents that the localized stress near the notches is significantly larger than the other sections in the out-of-plane rigid response, as shown in Fig. 7(b)-7(c). It can be seen that although the out-of-plane rigid stage is mainly a material property governed

process, the stress concentration effect also appears in this stage, making a more complex deformation process than stage I and stage II. The localized stress initiates cracks, leading to the final fracture of the kirigami metallic glass. The stress concentration, the phenomenon in which the maximum stress occurs at the edge of the notches, affects the ultimate load force of the out-of-plane rigid stage during the kirigami response. The intensity of the stress concentration is expressed as follows:

$$K = \sigma_{max.} / \sigma_{nom.} \tag{22}$$

where K is the stress concentration factor; σ_{norm} is nominal stress across the rectangular plate, and $\sigma_{nom.} = F_{appl.}/(ct_1)$, where $F_{appl.}$ is the applied force in plate, ct_1 is net area of the cross-section, c is taken as $(L_1' - L_1'')$ in the out-of-plane rigid deformation stage, i.e. $c = U_0$, as shown in Fig. 2(a); $t_1 \sim 2U_0$ in the out-of-plane rigid stage; $\sigma_{max.}$ is the stress that concentrates around the rectangle edge, $\sigma_{max.} \propto F_{rec.}/(c't_1')$, where $c' = 2r'$, which is shown in Fig. 1(a), and $t_1' = L_1''$ in this study. Referring to $K = 0.780 + 2.243\sqrt{L_1''/r'}$ $(1 \le L_1''/r' \le 361)$ [48], the intensity of the force concentration in this study is given as follows:

$$F_{rec.}/F_{III_{appl.}} = (c't_1'/ct_1)*(0.780 + 2.243\sqrt{L_1''/r'}) \quad (31 \le L_1''/r' \le 181) \tag{23}$$

Considering $2.243\sqrt{L_1''/r'} \gg 0.780$ in this study, equation (23) can be expressed as follows:

$$F_{rec.}/F_{III_{appl.}} \propto U_0^{-0.5} \tag{24}$$

also as $F_{III_{appl.}} \propto F_{rec.} U_0^{0.5}$

The concentrated force around the notch of a kirigami rectangle, i.e. $F_{rec.}$, leads to the tear of the kirigami pattern until the cracks propagate and coalesce to the nearest kirigami pattern. Then fracture occurs. The equation (24) indicates that the larger the kirigami unit size the smaller the intensity of force concentration, i.e., if the absolute applied force of the out-of-plane rigid deformation stage is the same, a smaller force would concentrate on the notch of kirigami unit rectangle. If a tear is stimulated around the kirigami rectangle where the concentrated force is larger than in other areas, a larger

absolute applied force would be needed for the sample with smaller intensity of force concentration. Thus, through affecting the intensity of the force concentration, the sample with a larger kirigmi unit size associates with a larger absolute applied load, i.e. a larger fracture-driven force, in general.

The smaller the kirigami unit size, the smaller the absolute force in the out-of-plane rigid deformation stage, contributing to a smaller fracture force in the whole tension process, although the samples with small kirigami unit size show large transition force in both the in-plane deformation stage and out-of-plane soft deformation stage. It indicates that the out-of-plane rigid deformation has a larger effect on the kirigami mechanical response than the former two stages. In the out-of-plane rigid deformation stage, the absolute force scales with U_0^{α}, i.e., $\left(F_{III_{ult.}} - F_{II_{ult.}}\right) \propto U_0^{\alpha}$, where $\alpha > 0$, as shown in Fig. 5(c). In this study, α is taken as (0.41 $\pm$ 0.07), which supports the concentrated force analysis, i.e. $F_{III_{appl.}} \propto F_{rec.} U_0^{0.5}$.

Considering the fitting functions of the absolute force of the three stages in the kirigami tension response, the fracture force in the kirigami mechanical response can be taken as:

$$F_{all} = (C_1 + C_2) * U_0^{-1} + C_3 * U_0^{\alpha} \quad (25)$$

The former two stages (in-plane deformation and out-of-plane soft deformation) are controlled by buckling and rotation of the kirigami patterns; while the last stage (out-of-plane rigid deformation) is mainly influenced by the material mechanical properties, especially the plasticity and fracture mechanism of the metallic glass which is controlled by the shear band behavior, affected by the force distribution. And, the former two stages and the last stage are affected by the kirigami unit size in opposite tendencies. The influence of the kirigami unit size on the out-of-plane rigid deformation plays a dominant role in the whole kirigami deformation response, at least at the microscale, i.e. within the unit size from 150 μm to 900 μm. When decreasing or increasing the kirigami unit size to other length scales, the predicted models of stage I and stage II at the microscale might be still appropriate since the beam deflection theorem doesn't change with length scales. It should be mentioned that the effect of the

seam is neglected in our study since the seam width, i.e., 2r, is too small, compared with the kirigami unit size (U_0), to influence the mechanical response. If the kirigami unit size decreases to near the seam width, the developed force prediction models of stage I and stage II would be modified. In addition, when the kirigami unit size decreases to the sub-micrometer or even nanometer scale, e.g. decreases to the metallic glass intrinsic length, ~ 1 μm [50], or even smaller than the critical length scale for shear band nucleating, ~ 20 nm [51], the relationship between the unit size and the fracture-driven force, i.e., the absolute force of stage III would become different from that at micro-meter scale. As a reflection of the metallic glass plasticity and fracture behavior, the absolute ultimate-force of stage III is mainly affected by the shear band nucleation and propagation process [52-57]. When the samples in the hundreds of micrometers and even larger scales, such as in this study, the plastic process is controlled by the propagation of the heterogeneous nucleated shear band in general [58], with weak size-dependence of strength. When decreasing the kirigami unit size to the sub-micrometer scale, but above shear band nucleation scale, shear band nucleation in a heterogeneous state controls the plastic deformation [52, 59], and contributes to a different fitting function in stage III. When the metallic glass sample decreases to the nanoscale, the heterogeneous nucleation of the flow units transform into homogeneous nucleation, because the flaws at this length scale are too small for potent heterogeneous nucleation [52]. At this scale, the homogenous flow unit nucleation would lead to a different deformation process from the deformation response controlled by in-homogenous shear band nucleation and shear band propagation in stage III during the kirigami-inspired tension, and it is very worthy of further experimental studies.

6. Conclusions

This work investigates the critical transition in the kirigami-inspired deformation process of metallic glass. The conclusions are summarized as follows:

- The kirigami pattern and the intrinsic mechanical properties of the materials affect the critical response in kirigami-inspired deformation. The in-plane deformation stage and the out-of-plane soft deformation stage are mainly affected by the geometric features, i.e. thickness, width or length of the kirigami pattern, and the

column number of the kirigami unit, according to the critical force prediction formula in this study. The out-of-plane rigid deformation stage, affected by shear band dynamics, is mainly controlled by the intensity of the force concentration based on the fracture process.

- The larger the kirigami unit size, the larger the transition load in the in-plane deformation stage and the out-of-plane soft deformation stage.
- The larger kirigami unit-size sample with smaller intensity of force concentration factor contributes to a larger absolute force in the out-of-plane rigid deformation. The last stage, i.e., the out-of-plane rigid deformation process, has larger effects on the final load force than the former two stages during the kirigami deformation response, contributing to the phenomenon that the larger the kirigami unit size, the larger the fracture force.

By introducing the beam deflection theory and the stress concentration factor, the study enables a prediction of the kirigami deformation response and contributes to optimum kirigami metallic glass design, opening up the possibility of the application of metallic glass with kirigami patterns in reversible and reconfigurable fields.

ACKNOWLEDGEMENTS

The authors gratefully acknowledge the financial support of the Research Grants Council of the Hong Kong Special Administrative Region, China (Project No. PolyU 15222017). The authors also gratefully acknowledge the Industrial Center of Hong Kong Polytechnic University and Mr. Sidney Wong for the technical support on Photochemical Machining.

REFERENCES

[1] A.A. Deleo, J. O'Neil, H. Yasuda, M. Salviato, J. Yang, Origami-based deployable structures made of carbon fiber reinforced polymer composites, Compos. Sci. Technol. 191 (2020) 108060.

[2] C. Coulais, E. Teomy, K. De Reus, Y. Shokef, M. Van Hecke, Combinatorial design of textured mechanical metamaterials, Nature 535 (2016) 529.

[3] F. Pan, Y. Li, Z. Li, J. Yang, B. Liu, Y. Chen, 3D Pixel Mechanical Metamaterials, Adv. Mater. 31 (2019) 1900548.

[4] T.A. Hewage, K.L. Alderson, A. Alderson, F. Scarpa, Double‐Negative Mechanical Metamaterials Displaying Simultaneous Negative Stiffness and Negative Poisson's Ratio Properties, Adv. Mater. 28 (2016) 10323-10332.

[5] L. Mizzi, E. Salvati, A. Spaggiari, J.-C. Tan, A.M. Korsunsky, Highly stretchable two-dimensional auxetic metamaterial sheets fabricated via direct-laser cutting, Int. J. Mech. Sci. 167 (2020) 105242.

[6] X. Ning, X. Wang, Y. Zhang, X. Yu, D. Choi, N. Zheng, D.S. Kim, Y. Huang, Y. Zhang, J.A. Rogers, Assembly of advanced materials into 3D functional structures by methods inspired by origami and kirigami: a review, Adv. Mater. Interfaces 5 (2018) 1800284.

[7] D.G. Hwang, K. Trent, M.D. Bartlett, Kirigami-inspired structures for smart adhesion, ACS Appl. Mater. Inter. 10 (2018) 6747-6754.

[8] A. Rafsanjani, K. Bertoldi, Buckling-induced kirigami, Phys. Rev. Lett. 118 (2017) 084301.

[9] J.J. Park, P. Won, S.H. Ko, A Review on Hierarchical Origami and Kirigami Structure for Engineering Applications, Int. J. Pr. Eng. Man.-G.T. 6 (2019) 147-161.

[10] B.M. Li, I. Kim, Y. Zhou, A.C. Mills, T.J. Flewwellin, J.S. Jur, Kirigami-Inspired Textile Electronics: KITE, Adv. Mater. Technol. 4 (2019) 1900511.

[11] A. Lamoureux, K. Lee, M. Shlian, S.R. Forrest, M. Shtein, Dynamic kirigami structures for integrated solar tracking, Nat. Commun. 6 (2015) 8092.

[12] N.S. Jang, K.H. Kim, S.H. Ha, S.H. Jung, H.M. Lee, J.M. Kim, Simple approach to high-performance stretchable heaters based on kirigami patterning of conductive paper for wearable thermotherapy applications, ACS Appl. Mater. Inter. 9 (2017) 19612-19621.

[13] M.K. Blees, A.W. Barnard, P.A. Rose, S.P. Roberts, K.L. McGill, P.Y. Huang, A.R. Ruyack, J.W. Kevek, B. Kobrin, D.A. Muller, Graphene kirigami, Nature 524 (2015) 204.

[14] R.M. Neville, J.G. Chen, X.G. Guo, F.H. Zhang, W.X. Wang, Y. Dobah, F. Scarpa,

J.S. Leng, H.X. Peng, A Kirigami shape memory polymer honeycomb concept for deployment, Smart Mater. Struct. 26 (2017) 05LT03.

[15] Y. Liu, B. Shaw, M.D. Dickey, J. Genzer, Sequential self-folding of polymer sheets, Sci. Adv. 3 (2017) e1602417.

[16] S. Lin, X. Liu, J. Liu, H. Yuk, H.C. Loh, G.A. Parada, C. Settens, J. Song, A. Masic, G.H. McKinley, Anti-fatigue-fracture hydrogels, Sci. Adv. 5 (2019) eaau8528.

[17] H.W. Sheng, W.K. Luo, F.M. Alamgir, J.M. Bai, E. Ma, Atomic packing and short-to-medium-range order in metallic glasses, Nature 439 (2006) 419.

[18] W.H. Wang, Metallic glasses: Family traits, Nat. Mater. 11 (2012) 275-276.

[19] X. Bian, D. Zhao, J. Kim, D. Şopu, G. Wang, R. Pippan, J. Eckert, Controlling the distribution of structural heterogeneities in severely deformed metallic glass, Mater. Sci. Eng. A 752 (2019) 36-42.

[20] S.H. Chen, K.C. Chan, T.M. Yue, F.F. Wu, Highly stretchable kirigami metallic glass structures with ultra-small strain energy loss, Scripta Mater. 142 (2018) 83-87.

[21] S.H. Chen, K.C. Chan, D.X. Han, L. Zhao, F.F. Wu, Programmable super elastic kirigami metallic glasses, Mater. Design 169 (2019) 107687.

[22] T.C. Shyu, P.F. Damasceno, P.M. Dodd, A. Lamoureux, L. Xu, M. Shlian, M. Shtein, S.C. Glotzer, N.A. Kotov, A kirigami approach to engineering elasticity in nanocomposites through patterned defects, Nat. Mater. 14 (2015) 785.

[23] Y. Tang, G. Lin, L. Han, S. Qiu, S. Yang, J. Yin, Design of Hierarchically Cut Hinges for Highly Stretchable and Reconfigurable Metamaterials with Enhanced Strength, Adv. Mater. 27 (2015) 7181-7190.

[24] Y. Tang, J. Yin, Design of cut unit geometry in hierarchical kirigami-based auxetic metamaterials for high stretchability and compressibility, Extreme Mech. Lett. 12 (2017) 77-85.

[25] Z. Qi, D.K. Campbell, H.S. Park, Atomistic simulations of tension-induced large deformation and stretchability in graphene kirigami, Phys. Rev. B 90 (2014) 245437.

[26] C. Zhou, S. Ming, T. Li, B. Wang, M. Ren, The Energy Absorption Behavior of Cruciforms Designed by Kirigami Approach, J. Appl. Mech. 85 (2018) 121008.

[27] F. Scarpa, M. Ouisse, M. Collet, K. Saito, Kirigami auxetic pyramidal core:

mechanical properties and wave propagation analysis in damped lattice, J. Vib. Acoust. 135 (2013) 041001.

[28] M. Moshe, E. Esposito, S. Shankar, B. Bircan, I. Cohen, D.R. Nelson, M.J. Bowick, Kirigami mechanics as stress relief by elastic charges, Phys. Rev. Lett. 122 (2019) 048001.

[29] M. Moshe, E. Esposito, S. Shankar, B. Bircan, I. Cohen, D.R. Nelson, M.J. Bowick, Nonlinear mechanics of thin frames, Phys. Rev. E 99 (2019) 013002.

[30] R. Sahingoz, M. Erol, M.R. Gibbs, Observation of changing of magnetic properties and microstructure of metallic glass Fe78Si9B13 with annealing, J. Magn. Magn. Mater. 271 (2004) 74-78.

[31] X.F. Li, S.X. Liang, X.W. Xi, Z. Jia, S.K. Xie, H.C. Lin, J.P. Hu, L.C. Zhang, Excellent performance of Fe78Si9B13 metallic glass for activating peroxymonosulfate in degradation of naphthol green B, Metals 7 (2017) 273.

[32] W.F. Yang, Y. Liu, Investigations of mechanical and shielding properties of Fe78Si9B13 amorphous thin ribbons, Mater. Rev. 10 (2009) 52-55.

[33] X.F. Li, K.F. Zhang, G.F. Wang, W.B. Han, Plastic deformation behavior of amorphous Fe78Si9B13 alloy at elevated temperature, J. Non-Cryst. Solids 354 (2008) 1061-1065.

[34] Y.H. Liu, C.T. Liu, W. Wang, A. Inoue, T. Sakurai, M. Chen, Thermodynamic origins of shear band formation and the universal scaling law of metallic glass strength, Phys. Rev. Lett. 103 (2009) 065504.

[35] J. Fornell, S. González, E. Rossinyol, S. Suriñach, M.D. Baró, D.V. Louzguine-Luzgin, J.H. Perepezko, J. Sort, A. Inoue, Enhanced mechanical properties due to structural changes induced by devitrification in Fe–Co–B–Si–Nb bulk metallic glass, Acta Mater. 58 (2010) 6256-6266.

[36] M. Mijalkovic, M. Trajkovic, B. Milosevic, Limit analysis of beams under combined stresses, FU Arch. Civ. Eng. 6 (2008) 75-88.

[37] G. Kaklauskas, J. Ghaboussi, Stress-strain relations for cracked tensile concrete from RC beam tests, J. Struct. Eng. 127 (2001) 64-73.

[38] J. Zhang, M. Ashby, Buckling of honeycombs under in-plane biaxial stresses, Int. J.

Mech. Sci. 34 (1992) 491-509.

[39] S. Prabhakaran, K. Chinnarasu, M.S. Kumar, Design and fabrication of composite bumper for light passenger vehicles, Int. J. Modern Eng. Res. 2 (2012) 2552-2556.

[40] J.M. Gere, S.P. Timoshenko, H. Saunders, Mechanics of materials, eight ed, CL Engineering, Canada, 2012.

[41] Y.S. Li, W. Shan, H.Y. Shen, Z.W. Zhang, J.Z. Liu, Bending resistance of I-section bamboo–steel composite beams utilizing adhesive bonding, Thin Wall. Struct. 89 (2015) 17-24.

[42] H.Y. Shi, W.Q. Liu, H. Fang, Y. Bai, D. Hui, Flexural responses and pseudo-ductile performance of lattice-web reinforced GFRP-wood sandwich beams, Compos. Part B-Eng. 108 (2017) 364-376.

[43] J.H. Zar, Calculation and miscalculation of the allometric equation as a model in biological data, Bioscience 18 (1968) 1118-1120.

[44] J.F. White, S.J. Gould, Interpretation of the coefficient in the allometric equation, Am. Nat. 99 (1965) 5-18.

[45] M. Vangbo, An analytical analysis of a compressed bistable buckled beam, Sensors Actuat. A-Phys. 69 (1998) 212-216.

[46] S.A. Zirbel, K.A. Tolman, B.P. Trease, L.L. Howell, Bistable mechanisms for space applications, PLoS One 11 (2016) e0168218.

[47] J. Chopin, V. Démery, B. Davidovitch, Roadmap to the morphological instabilities of a stretched twisted ribbon, J. Elast. 119 (2016) 137-189.

[48] F.I. Baratta, D.M. Neal, Stress-concentration factors in u-shaped and semi-elliptical edge notches, J. Strain Anal. Eng. 5 (1970) 121-127.

[49] F.G. Nelson, P.E. Schilling, J.G. Kaufman, The effect of specimen size on the results of plane-strain fracture-toughness tests, Eng. Fract. Mech. 4 (1972) 33-50.

[50] F.C. Li, S. Wang, Q.F. He, H. Zhang, B. Sun, Y. Lu, Y. Yang, The stochastic transition from size dependent to size independent yield strength in metallic glasses, J. Mech. Phys. Solids 109 (2017) 200-216.

[51] Q.K. Li, M. Li, Assessing the critical sizes for shear band formation in metallic glasses from molecular dynamics simulation, Appl. Phys. Lett. 91 (2007) 231905.

[52] J.R. Greer, J.T.M. De Hosson, Plasticity in small-sized metallic systems: Intrinsic versus extrinsic size effect, Prog. Mater. Sci. 56 (2011) 654-724.

[53] D.X. Han, G. Wang, J.L. Ren, L.P. Yu, J. Yi, I. Hussain, S.X. Song, H. Xu, K.C. Chan, P.K. Liaw, Stick-slip dynamics in a Ni62Nb38 metallic glass film during nanoscratching, Acta Mater. 136 (2017) 49-60.

[54] A.L. Greer, Y.Q. Cheng, E. Ma, Shear bands in metallic glasses, Mater. Sci. Eng. R 74 (2013) 71-132.

[55] D.X. Han, G. Wang, J. Li, K.C. Chan, S. To, F.F. Wu, Y.L. Gao, Q.J. Zhai, Cutting Characteristics of Zr-Based Bulk Metallic Glass, J. Mater. Sci. Technol. 31 (2015) 153-158.

[56] S. Ogata, F. Shimizu, J. Li, M. Wakeda, Y. Shibutani, Atomistic simulation of shear localization in Cu-Zr bulk metallic glass, Intermetallics 14 (2006) 1033-1037.

[57] D. Şopu, S. Scudino, X. Bian, C. Gammer, J. Eckert, Atomic-scale origin of shear band multiplication in heterogeneous metallic glasses, Scripta Mater. 178 (2020) 57-61.

[58] F.F. Wu, Z.F. Zhang, S.X. Mao, Size-dependent shear fracture and global tensile plasticity of metallic glasses, Acta Mater. 57 (2009) 257-266.

[59] A. Cao, Y. Cheng, E. Ma, Structural processes that initiate shear localization in metallic glass, Acta Mater. 57 (2009) 5146-5155.

Figure and table captions

Fig. 1 The details of kirigami pattern. (a) Representative pattern: $L_1 = 12L_0$, $L_2 = 6.5L_0$, $L_0 = U_0$, 2r = 0.06 mm, W = 8 mm; (b)-(k) corresponding to unit sizes of 150 μm, 225 μm, 300 μm, 375 μm, 450 μm, 525 μm, 600 μm, 675 μm, 750 μm, and 900 μm, respectively.

Fig. 2 Beam deflection analysis. (a) Schematic of kirgami-inspired tension; (b)

Schematic of kirgami-inspired rhombic unit in the tensile response; (c) Schematic of beam in the tensile response; (d) Extracted beam unit in the tensile response.

Fig. 3 Tension curve of kirigami metallic glass with the corresponding morphology. (a) The kirigami-inspired strain-force curve. Insert shows the enlarged strain-load curve corresponding to the region covered by dash line and the side view of the samples during in-plane stage and out-of-plane stages; (b) The front view of the sample during in-plane deformation stage; (c) The front view of the sample during out-of-plane soft deformation stage; (d) The front view of the sample during out-of-plane rigid deformation stage.

Fig. 4 The load-strain curves of kirigami metallic glass. (a) Repeat tests of different kirigami patterns; (b) Representative test of different kirigami patterns. Insert shows the enlarged curve corresponding to the region covered by dash line. The labels of 150, 225, 300, 375, 450, 525, 600, 675, 750, 900 corresponds to the kirigami unit size, U_0, of 150 μm, 225 μm, 300 μm, 375 μm, 450 μm, 525 μm, 600 μm, 675 μm, 750 μm, and 900 μm, respectively. The labels of a, b, and c correspond to different tensile samples with same kirigami unit size.

Fig. 5 Log-Log curve of (a) Absolute load of stage I - kirigami unit size; (b) Absolute load of stage II - kirigami unit size; (c) Absolute load of stage III - kirigami unit size. The experimental data are fitted with function $y = ax^b$ by red line, while black scatter squares represent the experimental data.

Fig. 6 The mechanical response of load-strain slope of stage II as a function of kirigami unit size.

Fig. 7 (a) Experimental and stimulated kirigami-inspired strain-force curve; (b) Finite element method (FEM) simulation shows the front view and side view of the stress distribution of the tensile sample during the out-of-plane rigid deformation stage; (c) FEM simulation shows the enlarged images of the stress concentration regions circled by black rectangle in (b).

Table list:

Table 1 The absolute soft-rigid transformation strain in the out-of-plane deformation, $(\varepsilon_{II_{ult.}} - \varepsilon_{I_{ult.}})_{ave.}$ is the average absolute strain in the out-of-plane soft stage of the repeated tests, $(\varepsilon_{II_{ult.}} - \varepsilon_{I_{ult.}})_{std.}$ is the stdev of absolute strain in the out-of-plane soft stage of the repeated tests.

Unit Size (μm)	150	225	300	375	450	525	600	675	750	900
$\xi_{ave.}$ (%)	153.08	109.36	117.60	109.54	114.83	116.17	102.34	103.56	109.51	117.03
$\xi_{std.}$ (%)	10.77	3.80	6.68	11.86	9.45	6.46	8.56	5.28	5.07	9.01

Figure list:

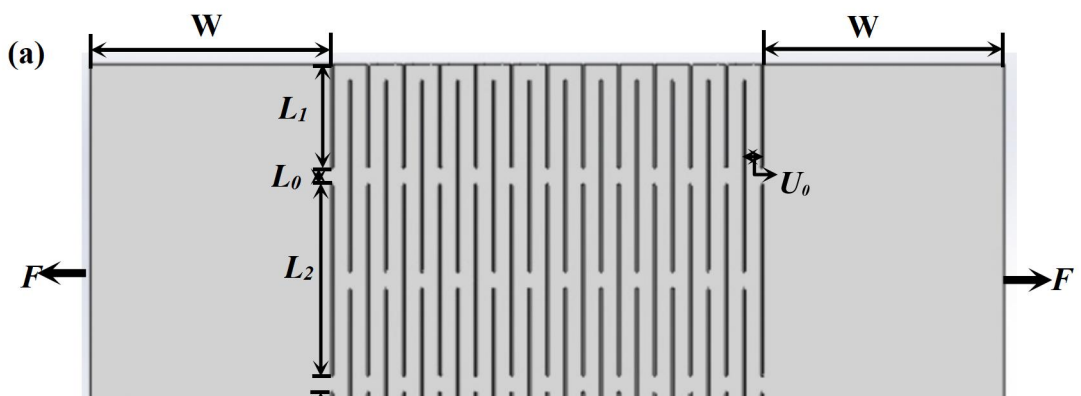

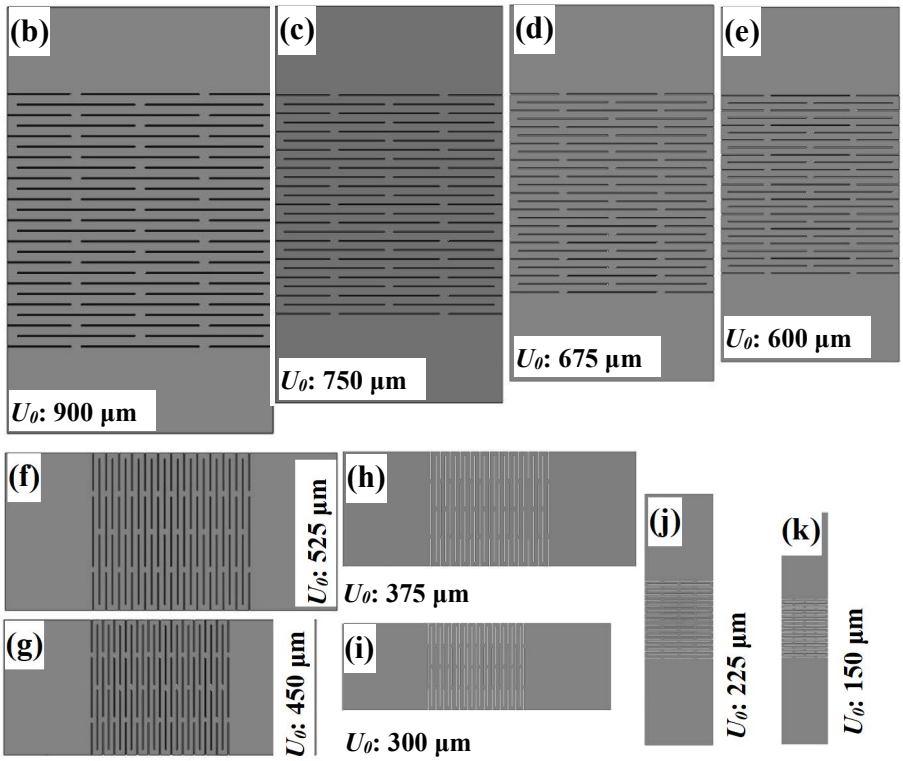

Fig. 1 The details of kirigami pattern. (a) Representative pattern: $L_1 = 12L_0$, $L_2 = 6.5L_0$, $L_0 = U_0$, 2r = 0.06 mm, W = 8 mm; (b)-(k) corresponding to unit sizes of 150 µm, 225 µm, 300 µm, 375 µm, 450 µm, 525 µm, 600 µm, 675 µm, 750 µm, and 900 µm, respectively.

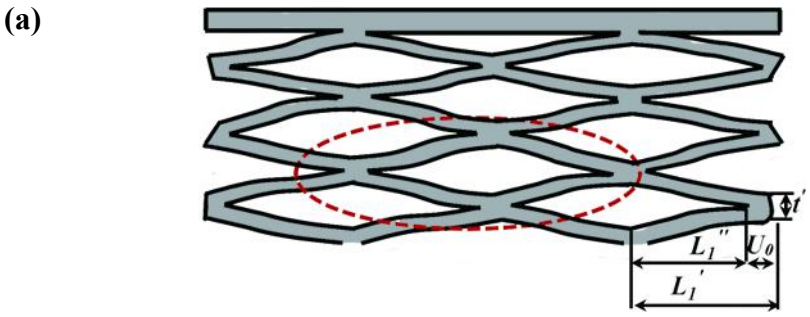

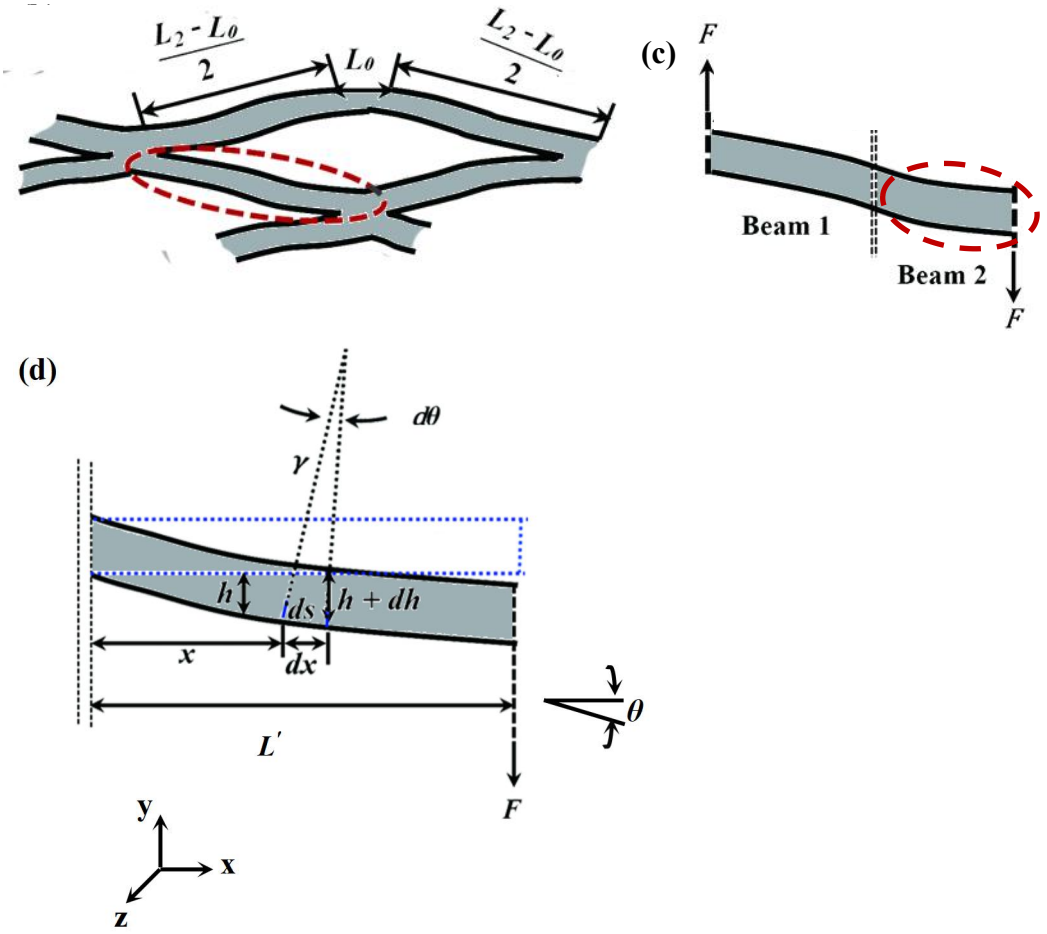

Fig. 2 Beam deflection analysis. (a) Schematic of kirgami-inspired tension; (b) Schematic of kirgami-inspired rhombic unit in the tensile response; (c) Schematic of beam in the tensile response; (d) Extracted beam unit in the tensile response.

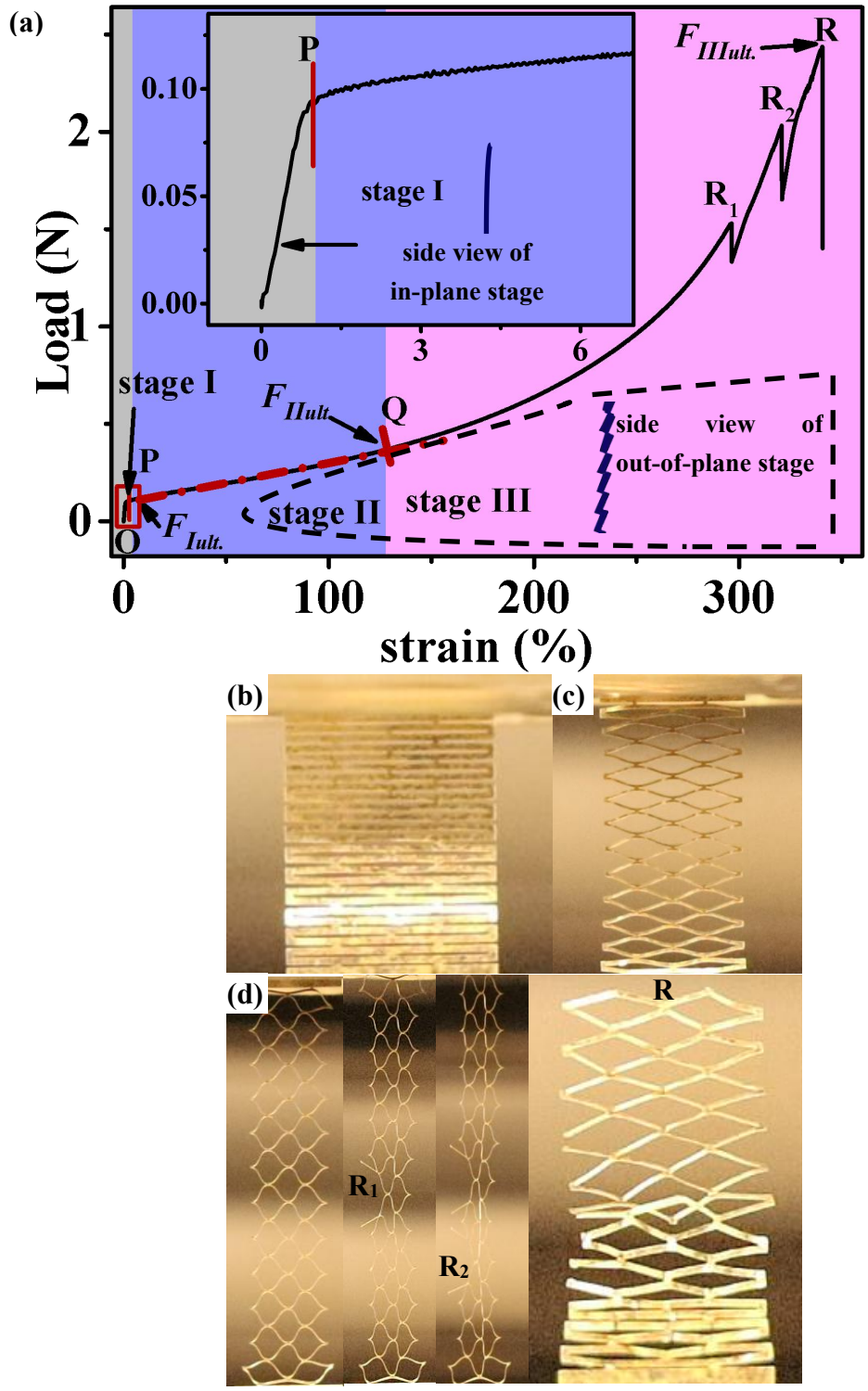

Fig. 3 Tension curve of kirigami metallic glass with the corresponding morphology. (a) The kirigami-inspired strain-force curve. Insert shows the enlarged strain-load curve corresponding to the region covered by dash line and the side view of the samples during in-plane stage and out-of-plane stages; (b) The front view of the sample during in-plane deformation stage; (c) The front view of the sample during out-of-plane soft deformation stage; (d) The front view of the sample during out-of-plane rigid deformation stage.

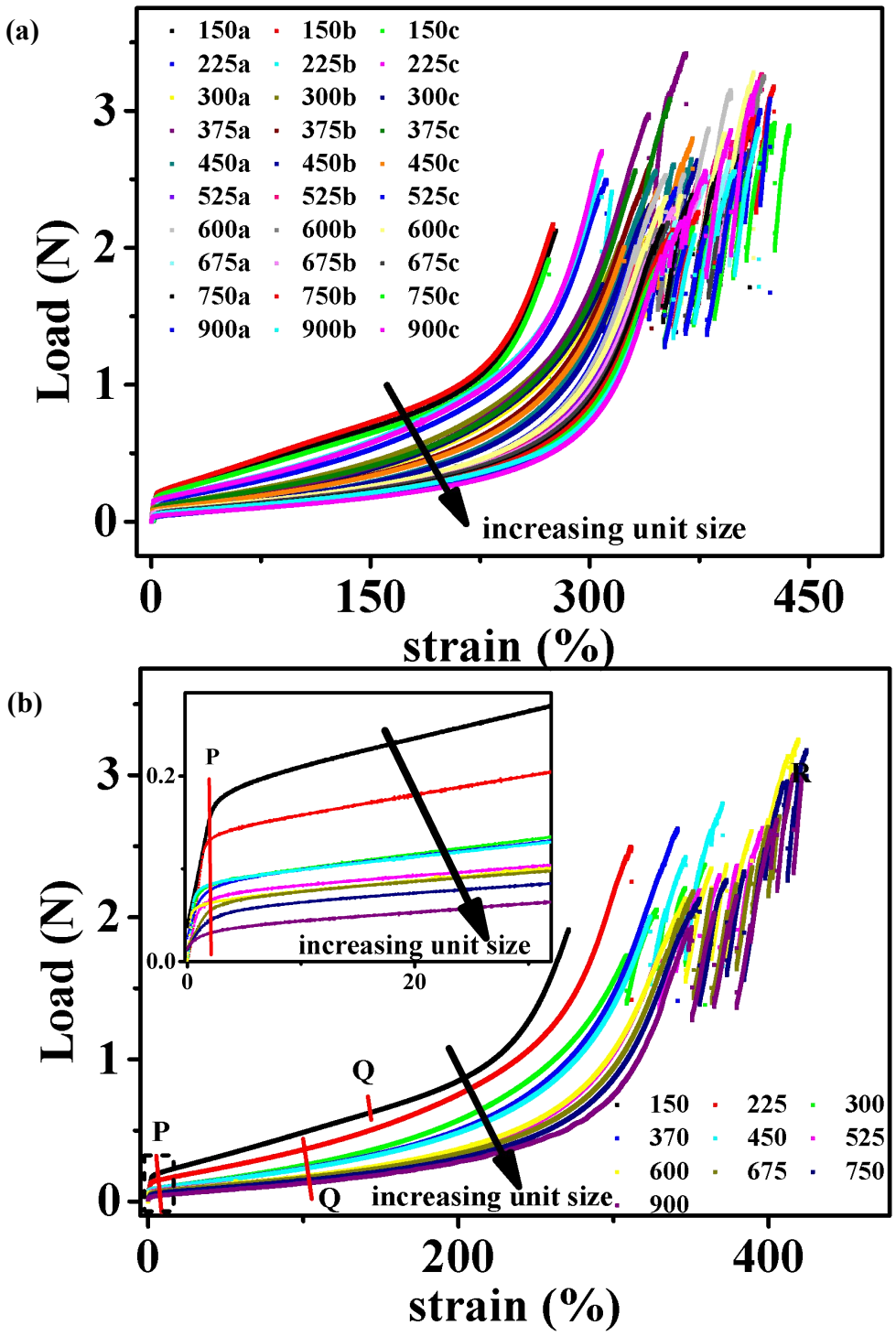

Fig. 4 The load-strain curves of kirigami metallic glass. (a) Repeat tests of different kirigami patterns; (b) Representative test of different kirigami patterns. Insert shows the enlarged curve corresponding to the region covered by dash line. The labels of 150, 225, 300, 375, 450, 525, 600, 675, 750, 900 corresponds to the kirigami unit size, U_0, of 150 μm, 225 μm, 300 μm, 375 μm, 450 μm, 525 μm, 600 μm, 675 μm, 750 μm, and 900 μm, respectively. The labels of a, b, and c correspond to different tensile samples with same kirigami unit size.

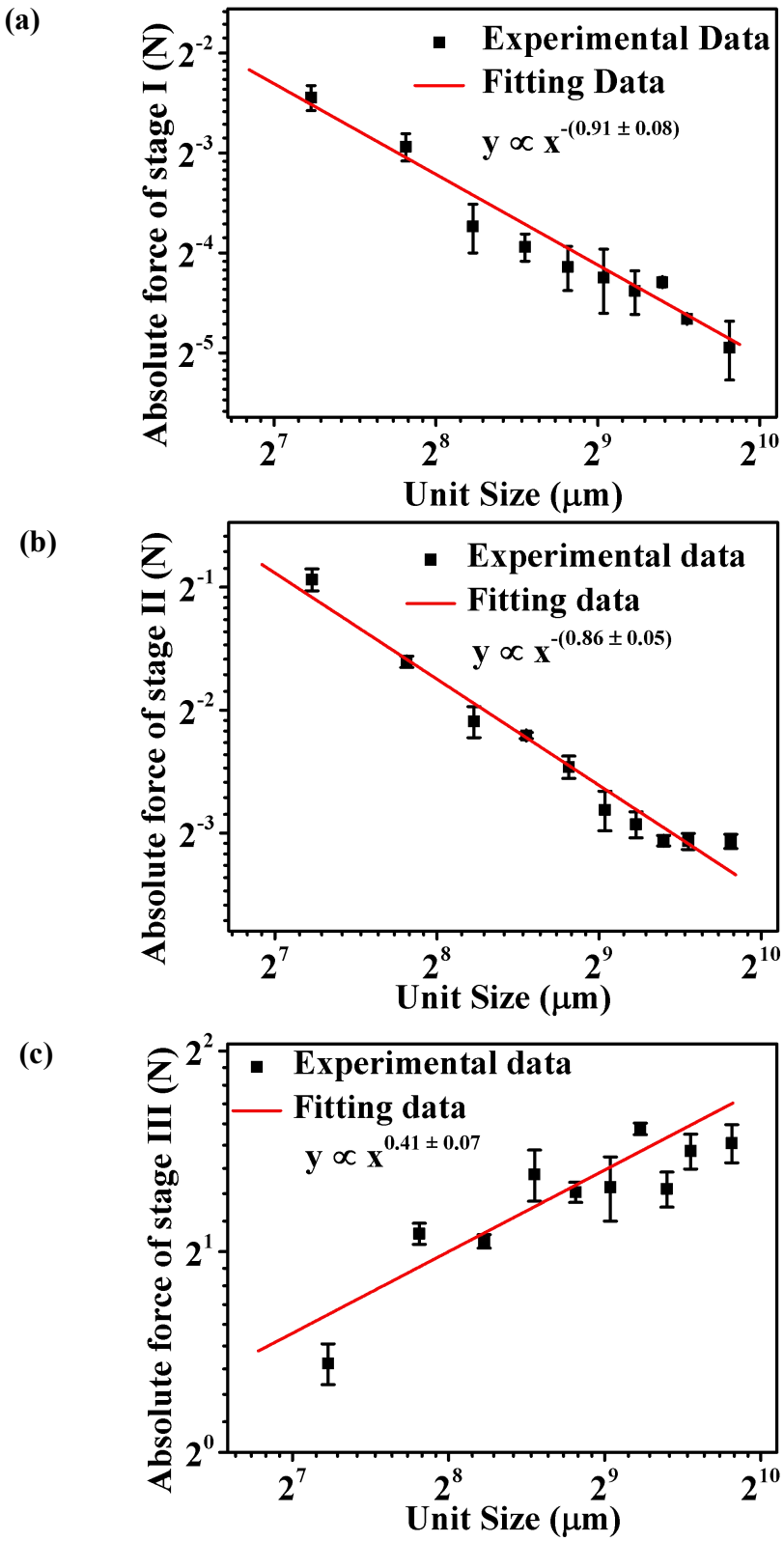

Fig. 5 Log-Log curve of (a) Absolute load of stage I - kirigami unit size; (b) Absolute load of stage II - kirigami unit size; (c) Absolute load of stage III - kirigami unit size. The experimental data are fitted with function $y = ax^b$ by red line, while black scatter squares represent the experimental data.

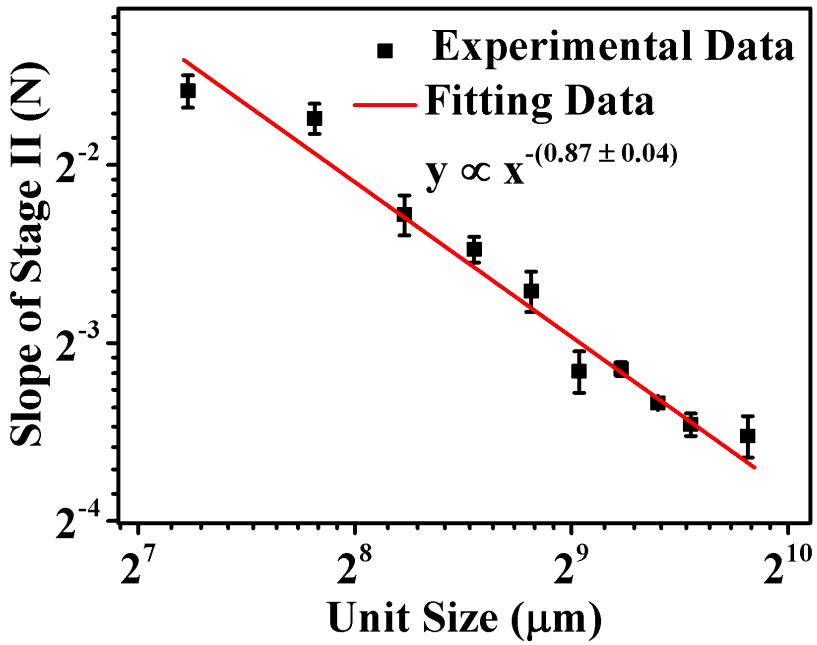

Fig. 6 The mechanical response of load-strain slope of stage II as a function of kirigami unit size.

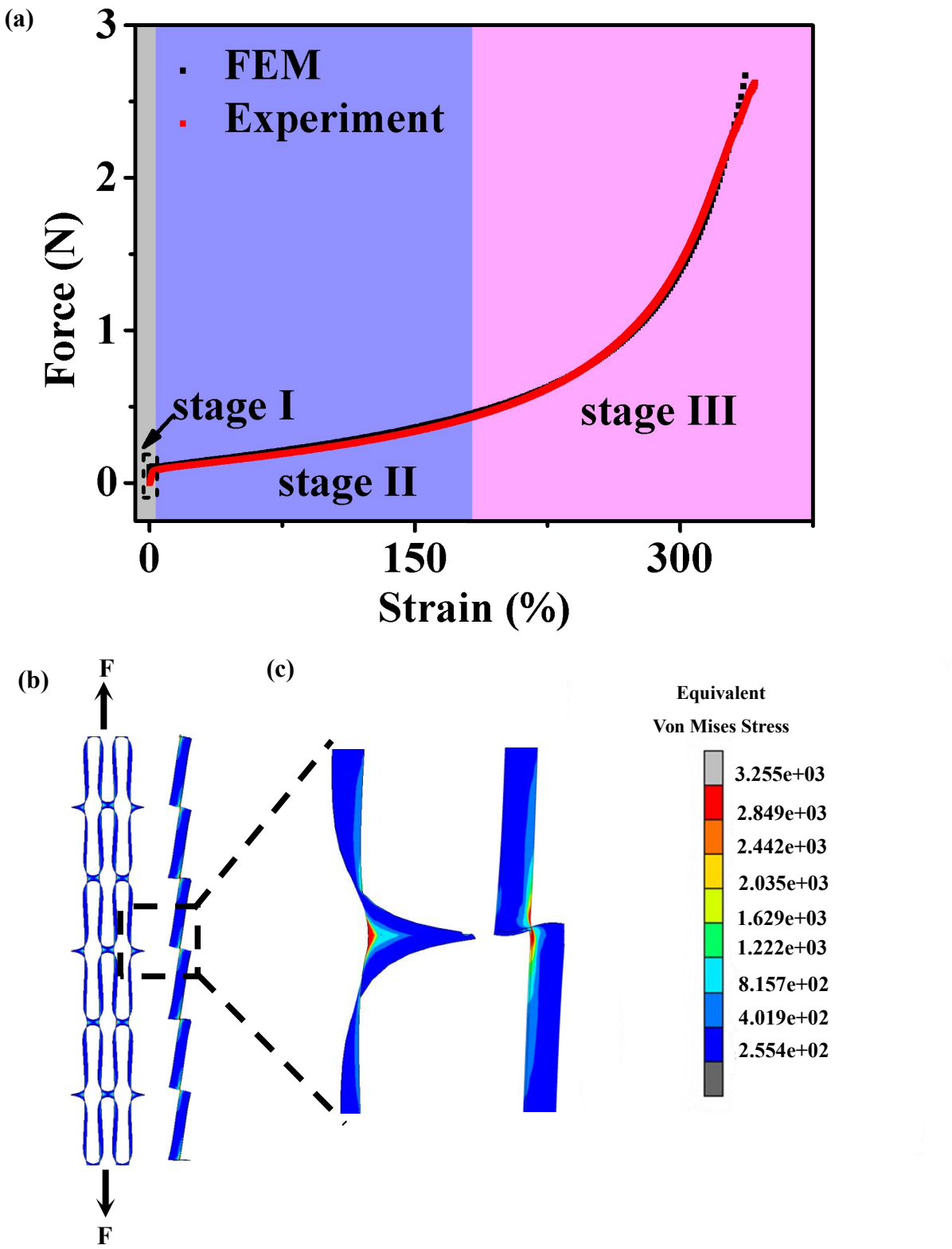

Fig. 7 (a) Experimental and stimulated kirigami-inspired strain-force curve; (b) Finite element method (FEM) simulation shows the front view and side view of the stress distribution of the tensile sample during the out-of-plane rigid deformation stage; (c) FEM simulation shows the enlarged images of the stress concentration regions circled by black rectangle in (b).